Sedimentation of an oblate ellipsoid in narrow tubes

Xin Yang, Haibo Huang,* and Xiyun Lu
Department of Modern Mechanics, University of Science and Technology of China, Hefei, Anhui 230026, China
(Received 2 August 2015; revised manuscript received 18 September 2015; published 8 December 2015)

Sedimentation behaviors of an oblate ellipsoidal particle inside narrow [$R/a \in (1.2,2.0)$] infinitely long circular tubes are studied by the lattice Boltzmann method, where R and a are the radius of the tube and the length of the semimajor axis of the ellipsoid, respectively. The Archimedes numbers (Ar) up to 70 are considered. Four periodic and two steady sedimentation modes are identified. It is the first time that the anomalous mode has been found in a circular tube for an ellipsoidal particle. The phase diagram of the modes as a function of Ar and R/a is obtained. The anomalous mode is observed in the larger R/a and lower-Ar regime. Through comparisons between the anomalous and oscillatory modes, it is found that $\frac{R}{a}$ plays a critical role for the anomalous mode. Some constrained cases with two steady modes are simulated. It is found that the particle settles faster in the unconstrained modes than in the corresponding constrained modes. This might inspire further study on why the particle adopts a specific mode under a certain circumstance.

DOI: 10.1103/PhysRevE.92.063009 PACS number(s): 47.55.Kf, 47.11.−j

I. INTRODUCTION

Motion of the particles in tubes are ubiquitous in nature and many applications in industries, such as chemical, biological, and mechanical engineering. Examples include the sedimentation of particles inside tubes, blood flow in the microcirculation, and capsules flowing through tubes or pipes [1,2]. Particle shapes play a critical role in determining the motions. In the following, the studies on the motion of particles are classified according to the particle shapes.

The motions of spherical particles have been studied extensively. There are many numerical studies on the movement of suspended spheres in the Couette flow [3] and tube flows [4]. There are also many experimental studies on spherical particles in Poiseuille flows. For example, Segre and Silberberg studied the migration of neutrally buoyant spheres inside tubes and found the Segre-Silberberg effect [5]. It was observed that the spherical particles migrate towards an equilibrium position and equilibrate at a distance of 0.6 times the radius of the tube from the tube's center [5]. This finding may be important in explaining certain flow behavior of the suspensions and may find application in the fractionation of particles of different size.

For the nonspherical particle, there are some studies on motions of rodlike particle or thin disk [6]. For example, Russel *et al.* investigated the motion of an inertialess rodlike object falling near a flat wall in the Stokes flow. They found that when the rod approaches a vertical wall, it rotates and thus turns away from the wall. They concluded that the rod will undergo a periodic oscillatory motion between two parallel plates [7]. There are also many studies on free falling of a disk. Zhong *et al.* [8] experimentally investigated the sedimentation of a free thin disk and new types of free falling motions were found for small moment of inertia values, including the spiral mode and transitional mode.

More recently, Rahmani and Wachs investigated the free falling of cubical and tetrahedral particles for different Reynolds numbers [9]. They found that mechanisms of path instabilities for angular particles are different from those for spherical ones. The rotation of the particle plays a more significant role in the transition to chaos for angular particles. However, in the study, only periodic lateral boundary conditions is applied. It suggested that the side wall effect is not considered.

For nonspherical particle, ellipsoidal particles attract more attention. Jeffery investigated the rotational modes of an ellipsoid in a Couette flow under Stokes flow conditions [10]. Yu *et al.* [11], Huang *et al.* [12], and Rosén [13] studied an ellipsoid in Couette flows with inertia. They found several rotational modes. As an extension, Huang *et al.* [14] investigated the intrinsic viscosities for prolate and oblate spheroidal suspensions. These studies may enrich our understanding of suspensions of ellipsoidal particles.

However, for more common cases in industry, particles are usually inside a tube. For example, Sugihara-Seki numerically studied the motions of an inertialess elliptical particle in tube Poiseuille flow using a finite-element (FE) method [1]. Several motion modes for prolate and oblate spheroids with $\mathrm{Re} = 0$ are found.

There are also some studies on sedimentation of ellipsoidal particle. Xia *et al.* studied the sedimentation of a non-neutrally buoyant elliptical particle in a two-dimensional (2D) channel with different block ratios at intermediate Re using the lattice Boltzmann method (LBM) [15]. They found five different modes: the oscillatory mode, the "anomalous" rolling mode, the vertical mode, the inclined mode, and the horizontal mode. For the oscillatory mode, the particle "wiggles" down the channel, oscillating around the centerline of the channel. For the vertical and horizontal modes, the particle sediments vertically and horizontally along the center of the 2D channel, respectively. For the inclined mode, the elliptical particle sediments off-center along a vertical line with an inclined orientation. For the anomalous rolling mode (or the anomalous mode), the elliptical particle rotates as if it is contacting and rolling up one of the walls when it travels down vertically. Although the 2D simulations may provide some useful information for the actually three-dimensional (3D) flows in a tube, results of 3D simulations may be significantly different from those of 2D simulations [16].

Swaminathan *et al.* studied the sedimentation of a 3D prolate spheroid inside an infinitely long tube at low

*huanghb@ustc.edu.cn

and intermediate Reynolds numbers using the arbitrary Lagrangian-Eulerian (ALE) based on the FE method [17]. They found the oscillatory, horizontal, and inclined modes. However, in the 3D study, the tube diameter is fixed to be 8 times the lengths of semimajor axis of the ellipsoid. Like in Ref. [17], previous investigations of sedimentation have mostly considered the case of wide tubes. Hence, the side wall effect or the particle-tube size ratio effect on the motion behavior of the particle is unknown. In this paper, the effects of wall boundaries on the mode of sedimentation are investigated in detail.

To investigate sedimentation behaviors of a prolate ellipsoid in narrow and infinitely long tubes, recently we carried out a numerical study [18]. In the study, the particle-tube size ratio effect was examined and two new modes: The spiral mode and the vertically inclined mode were found. The phase diagram of these modes for the prolate spheroid is also obtained.

In this paper we extend the numerical study to an oblate case to further investigate the effect of the particle geometry. Here the sedimentation behaviors of an oblate ellipsoidal particle are examined, which is also a typical particle geometry. In the meanwhile, the effects of wall boundaries are also taken into account. In this paper, some undisclosed features of an oblate particle sedimentation in a narrow tube are discussed.

Hence, the main emphasis in this work is to study the effect of wall boundaries on the flow patterns observed during sedimentation of an oblate ellipsoid. This study may shed some light on the sedimentation behaviors of particles.

The numerical method used in our study is based on the multiple-relaxation-time (MRT) LBM [19] and the dynamic multiblock strategy [18]. The LBM have been well established to study the motion of 3D ellipsoidal particle's inside Couette flow and sedimentation of 2D ellipsoid [12,15,20–22]. These studies all demonstrate that the LBM is a powerful tool to study the particulate movement in the fluids. The numerical methods are validated in Ref. [18]. In Sec. II, the MRT-LBM and basic equations for the motion of the solid particle are introduced briefly. A further validation is given in Sec. II C. The phase diagram is shown in Sec. IV A and the identified modes are discussed in Sec. IV B. Further discussions for the mechanism are presented in Sec. IV C. Finally, some concluding remarks are stated in Sec. V.

II. NUMERICAL METHOD

A. MRT-LBM

The MRT-LBM [23] is used to solve the fluid flow governed by the incompressible Navier-Stokes equations. The Lattice Boltzmann Equation (LBE) [19] can be written as

$$|f(\vec{x}+\vec{e}_i\delta t, t+\delta t)\rangle - |f(\vec{x},t)\rangle = -\mathbf{M}^{-1}\hat{\mathbf{S}}[|m(\vec{x},t)\rangle - |m^{\mathrm{eq}}(\vec{x},t)\rangle], \quad (1)$$

where Dirac notation of ket $|\cdot\rangle$ vectors symbolize the column vectors. $|f(\vec{x},t)\rangle$ represents the particle distribution function which has 19 component f_i with $i = 0,1,\ldots,18$ because the D3Q19 model is used in our 3D simulations. The collision matrix $\hat{\mathbf{S}} = \mathbf{M}\cdot\mathbf{S}\cdot\mathbf{M}^{-1}$ is diagonal with

$$\hat{\mathbf{S}} \equiv (0,s_1,s_2,0,s_4,0,s_4,s_9,s_{10},s_9,s_{10},s_{13},s_{13},s_{13},s_{16},s_{16},s_{16}), \quad (2)$$

where the parameters of $\hat{\mathbf{S}}$ are chosen as [19]: $s_1 = 1.19$, $s_2 = s_{10} = 1.4$, $s_4 = 1.2$, $s_9 = 1/\tau$, $s_{13} = s_9$, $s_{16} = 1.98$. $|m^{\mathrm{eq}}\rangle$ is the equilibrium value of the moment $|m\rangle$, where the moment $|m\rangle = \mathbf{M}\cdot|f\rangle$, i.e., $|f\rangle = \mathbf{M}^{-1}\cdot|m\rangle$. $\mathbf{M}$ is a 19×19 linear transformation matrix which is used to map the column vectors $|f\rangle$ in discrete velocity space to the column vectors $|m\rangle$ in moment space. The matrix $\mathbf{M}$ and $|m^{\mathrm{eq}}\rangle$ are same as those used by D'Humiere *et al.* [19] and Huang *et al.* [12]. In Eq. (1), $\vec{e}_i$ are the discrete velocities. For the D3Q19 velocity model,

$$\vec{e}_i = c\begin{bmatrix} 0 & 1 & -1 & 0 & 0 & 0 & 0 & 1 & 1 & -1 & -1 & 1 & -1 & 1 & -1 & 0 & 0 & 0 & 0 \\ 0 & 0 & 0 & 1 & -1 & 0 & 0 & 1 & -1 & 1 & -1 & 0 & 0 & 0 & 0 & 1 & 1 & -1 & -1 \\ 0 & 0 & 0 & 0 & 0 & 1 & -1 & 0 & 0 & 0 & 0 & 1 & 1 & -1 & -1 & 1 & -1 & 1 & -1 \end{bmatrix}, \quad (3)$$

where c is the lattice speed defined as $c = \frac{\Delta x}{\Delta t}$. In our study $\Delta x = 1$ lu and $\Delta t = 1$ ts, where lu, ts, and mu represent the lattice unit, time step, and mass unit, respectively. The macrovariables of fluid flow can be obtained from

$$\rho = \sum_i f_i, \quad \rho u_\alpha = \sum_i f_i e_{i\alpha}, \quad p = c_s^2\rho, \quad (4)$$

where subscript α denotes three coordinates. The parameter τ is related to the kinematic viscosity of the fluid: $\nu = c_s^2(\tau - 0.5)\Delta t$, where $c_s = \frac{c}{\sqrt{3}}$ is the sound speed.

B. Solid particle dynamics and fluid-solid boundary interaction

In our simulation, the oblate ellipsoid particle is described by

$$\frac{x'^2}{c^2} + \frac{y'^2}{b^2} + \frac{z'^2}{a^2} = 1, \quad (5)$$

where c, b, and a are the lengths of three semiprincipal axes of the particle in x', y', and z' axis of body-fixed coordinate system, respectively (see Fig. 1). The body-fixed coordinate system can be obtained by a combination of coordinate transformation around the $z'-x'-z'$ axis with Euler angles (ϕ,θ,ψ) from space-fixed coordinate system (x,y,z) which initially overlaps the body-fixed coordinate system. The combination of coordinate transformation is illustrated in Fig. 1. The evolution axis always overlaps the x' direction. The migration and rotation of the particle are determined by Newton's equation and Euler's equation,

$$m\frac{d\mathbf{U}(t)}{dt} = \mathbf{F}(t), \quad (6)$$

$$\mathbf{I}\cdot\frac{d\Omega(t)}{dt} + \Omega(t)\times[\mathbf{I}\cdot\Omega(t)] = \mathbf{T}(t), \quad (7)$$

respectively, where $\mathbf{I}$ is the inertial tensor and $\Omega(t)$ and $\mathbf{T}$(t) represent the angular velocity and the torque exerted on the

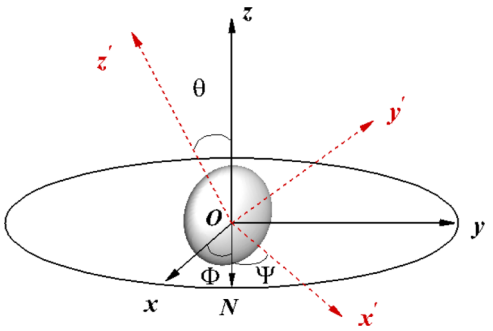

FIG. 1. (Color online) Schematic diagram of the combination of coordinate transformation from (x,y,z) to (x',y',z') with three Euler angles (ϕ,θ,ψ). Line "ON" represents the pitch line of (x,y) and (x',y') coordinate planes. Two coordinate systems are overlapping initially. First, the particle rotates around the z' axis with a recession angle ϕ and then the particle rotates around the new x' axis (i.e., line "ON") with a nutation angle θ. Finally, the particle rotates around the new z' axis with a angle of rotation ψ.

particle in the body-fixed coordinate system, respectively. In the frame, **I** is diagonal and the principal moments of inertial can be written as

$$I_{x'x'} = m\frac{b^2+a^2}{5}, \quad I_{y'y'} = m\frac{c^2+a^2}{5}, \quad I_{z'z'} = m\frac{c^2+b^2}{5}, \tag{8}$$

where $m = \frac{4}{3}\rho_p \pi abc$ is the mass of the particle. ρ_p is the density of the particle. It is not appropriate to solve Eq. (7) due to an inherent singularity [24]. Thus four quaternion parameters are used as generalized coordinates to solve the corresponding system of equations [22]. A coordinate transformation matrix with four quaternion parameters [22] is applied to transform corresponding item from the space-fixed coordinate system to the body-fixed coordinate system. With four quaternion parameters, Eq. (7) can be solved using a fourth-order accurate Runge-Kutta integration procedure [12].

In the simulations, the fluid-solid boundary interaction is based on the schemes of Aidun *et al.* [20] and Lallmand and Luo [23], which is an accurate moving-boundary treatment. The momentum exchange scheme is used to calculate the force exerted on the solid boundary. The forces due to the fluid nodes covering the solid nodes and the solid nodes covered by the fluid nodes [20] are also considered in the study.

To prevent the overlap of the particle and the wall, usually the repulsive force between the wall and particle should be applied [18]. Here the lubrication force model is identical to that we used in Ref. [18] and the validation of the force model has been tested extensively in Ref. [18].

C. Validation

Our LBM code has been validated in Ref. [18] by the cases of migrations of a neutrally buoyant sphere in tube Poiseuille flows [25] and a case of a prolate ellipsoid sedimentation in a circular tube [17]. To further validate our LBM code, the migration of a neutrally buoyant sphere in a tube Poiseuille flow [26] is also performed.

In the simulations, two kinds of the simulations are performed: unconstrained and constrained. In the unconstrained simulation, the particle is allowed to move and rotate freely. In the constrained simulation, the particle is allowed to rotate freely but only allowed to move along a line parallel to the axis of the tube [26].

In the simulations, the computational domain is 112 lu $\times$ 11 lu $\times$ 160 lu. The radii of the tube and the sphere are $R = 53.333$ lu and $r = 8$ lu, respectively (radius ratio 0.15). To make the simulations more efficient, the multiblock strategy is also used. The coarse and fine grids are $56 \times 56 \times 80$ and $112 \times 112 \times 50$, respectively. The fine grid is immersed in the coarse grid. The nondimensional relaxation time is $\tau_f = 0.8$, and $\tau_c = 0.65$. The pressure boundary conditions are applied in the two ends of the tube with $\Delta p = p_{\text{in}} - p_{\text{out}} = 0.002107$ mu/lu/ts^2. In the Poiseuille flow, the maximum velocity in the axis of the tube is $U_m = \frac{\Delta p R^2}{4\mu L} = 0.09364$ lu/ts, where the tube length $L = 160$ lu. Hence, in our simulations, $\text{Re} = \frac{8r^2 U_m}{\nu R} = 9.0$, which is identical to that in Ref. [26].

The equilibrium position r/R and U_z, Ω_x at equilibrium state are compared with results of [26] in Table I. Here the equilibrium position for the spherical particle inside the Poiseuille flow is very close to those obtained through ALE and DLM schemes. The velocity and angular velocity of the particle (U_z and Ω_x) and their normalized values (U_z' and Ω_x', which are normalized by U_m and $\frac{U_m}{D}$, respectively) are also illustrated in the table. It is seen that the normalized velocities of the particle obtained from the LBM simulation agree well with those obtained from the ALE and DLM schemes [26].

Figure 2 shows the results of the constrained cases. The normalized sedimentation velocity (U_z'), rotational velocity (Ω_x'), and lift force of the LBM simulation are compared with those obtained from the ALE and DLM. The lift force is normalized by $\rho U_m^2 R^2$. For U_z' and Ω_x', our results agree very well with those obtained from the ALE and DLM schemes [26]. For the lift force, our results are also well consistent with those given in Ref. [26]. Near $r/R = 0.6$, the sphere is at its equilibrium position, in which the resultant force is zero.

III. AN OBLATE ELLIPSOID SEDIMENTATION IN A TUBE

The sedimentation of an oblate ellipsoidal particle in infinitely long tubes is illustrated in Fig. 3. In this problem,

TABLE I. The equilibrium position r/R, and U_z, Ω_x at equilibrium state for unconstrained cases. The number in the square brackets indicates the value of the power of 10.

Scheme	r/R	U_z	Ω_x	U_m	D	U_z'	Ω_x'
LBM	0.600	0.0583 lu/ts	9.92[−4] ts^{-1}	0.0936 lu/ts	53.334 lu	0.623	0.5640
ALE	0.601	12.4 cm/s	4.65 s^{-1}	20 cm/s	2.5 cm	0.62	0.5813
DLM	0.606	12.2 cm/s	4.63 s^{-1}	20 cm/s	2.5 cm	0.61	0.5788

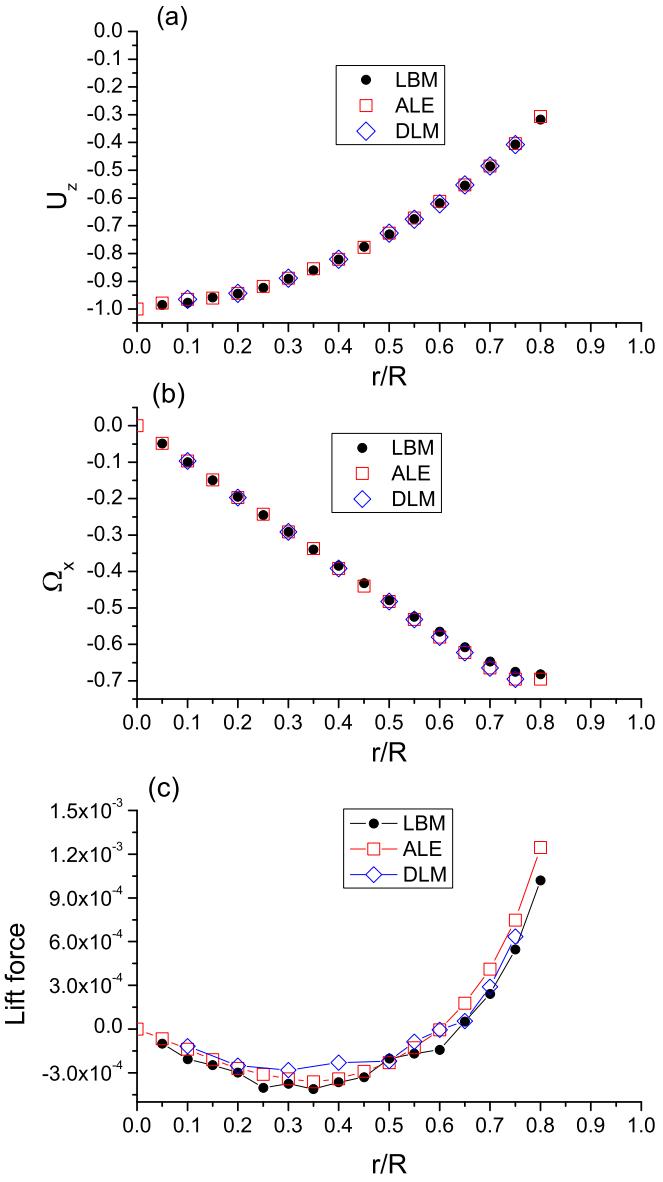

FIG. 2. (Color online) Constrained cases for a spherical particle moving inside a circular tube, the particle is allowed to rotate freely but only allowed to move along the line parallel to the axis of the tube. (a) Normalized velocity U_z', (b) normalized rotational velocity Ω_x', and (c) normalized lift force as functions of radial position. The ALE and DLM results come from Ref. [26].

D ($D = 2R$) denotes the diameter of the circular tube and only cases with $a = b = 2c$ are considered. The Reynolds number (Re) is defined as $\mathrm{Re} = \frac{2U_t a}{\nu}$, where U_t is the average terminal sedimentation velocity in the $-z$ direction. In the study, the gravity is considered in the $-z$ direction. The Archimedes number is defined as

$$\mathrm{Ar} = \sqrt{\frac{ga^3(\rho_p - \rho_f)}{\rho_f \nu^2}}, \tag{9}$$

where g is the acceleration of gravity and ρ_f and ρ_p denote the densities of the fluid and the particle, respectively.

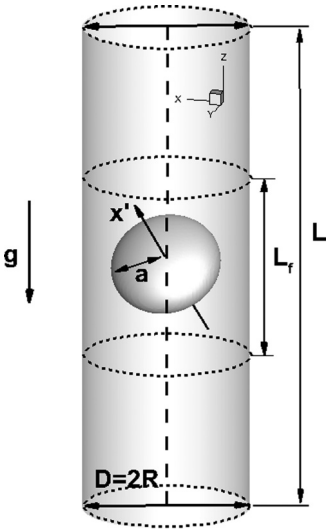

FIG. 3. Schematic diagram for the sedimentation of an oblate ellipsoid in a circular tube filled with viscous fluid.

In our study, we choose the oblate ellipsoid with $a = 0.05$ cm, $\nu = 0.01$ cm^2/s, and $g = 980$ cm/s^2. We have

$$\frac{ga^3}{\nu^2} = 1225, \tag{10}$$

which is fixed and Ar is only a function of $\frac{\rho_p}{\rho_f}$. Hence, the nondimensional parameters Ar and confinement ratio $\frac{R}{a}$, are dominated in this study. In the following cases, the oblate ellipsoid may be released from the central axis of the tube in the position $(0,0,\frac{L}{2} + \xi)$, where L is the tube length and ξ is a small distance. The initial velocities of flow field are zero and the density of the fluid is set to be $\rho_f = 1.0$. In our simulations, $L = 20D$ is adopted and the ellipsoidal particle is kept in the middle of the tube approximately all the times so as to minimized the end effects [18]. In most cases, the initial orientation of the ellipsoid is $(\phi,\theta,\psi) = (90^\circ,90^\circ,60^\circ)$, which means the angle between the evolution axis of the oblate particle (x') and tube axis is 60°.

Usually in our simulations, the semimajor axis of the oblate ellipsoid is represented by 20 lu, i.e., $a = 20$ lu and $\tau_f = 0.6$. For example, when we simulate the case of $\frac{R}{a} = 1.2$, the total mesh is about 50 lu $\times$ 50 lu $\times$ 960 lu. The grid-independent study and time-step-independent study have been performed and it is shown that the mesh size and the time step is sufficient to get accurate results.

IV. DISCUSSIONS

A. Phase diagram

A series of cases with different Ar and confinement ratio $\frac{R}{a}$ were simulated and several periodic or steady sedimentation modes are identified. The phase diagram in the ($\frac{R}{a}$, Ar) plane is obtained.

For each case with a specific $\frac{R}{a}$, and Ar, usually several simulations with different initial orientations and positions are performed. In all of our simulations, it is not found that the terminal mode depends on the initial positions or initial orientations of the particle. For example, eight simulations for

TABLE II. Eight different initial conditions for the case $\frac{R}{a} = 1.6$, Ar = 40, and $a = 20$ lu. All initial position in the z direction is $\frac{z}{R} = 20.02$, see Sec. III and Fig. 3 for more details.

Case	position $(\frac{x}{R}, \frac{y}{R})$	ϕ	θ	ψ
1	(0.1, 0.0)	90°	90°	60°
2	(−0.15, 0.0)	90°	15°	20°
3	(0.0, 0.1)	0°	45°	60°
4	(0.0, −0.2)	15°	10°	20°
5	(0.1, 0.3)	90°	90°	45°
6	(0.2, 0.2)	20°	10°	45°
7	(0.3, 0.2)	0°	45°	20°
8	(0.1, 0.4)	15°	20°	20°

the case $\frac{R}{a} = 1.6$, Ar = 40 with different initial orientations and positions are performed. The initial conditions are listed in Table II. All eight cases finally reach the spiral mode.

Figure 4 shows the snapshots of five typical modes: spiral, oscillatory, horizontal, inclined, and anomalous modes. More details for each mode are described in Sec. IV B.

The phase diagram is shown in Fig. 5. Several regimes for different modes are obtained. It is seen that the oscillatory mode occurs at a small confinement ratio $\frac{R}{a}$ and lower Ar. Hence, the oscillatory mode may be associated with strong wall effect. When $\frac{R}{a}$ is large enough, due to diminishing of the wall effect, the oscillatory mode may disappear. Instead, the inclined mode, the horizontal mode and the anomalous mode may occur. The critical Ar at which the oscillatory mode transfers to the inclined mode becomes lower as $\frac{R}{a}$ increases. The spiral mode appears mainly at moderate $\frac{R}{a}$ and high Ar. The spiral mode for the oblate ellipsoid is only observed in regime $1.2 > \frac{R}{a} > 1.8$. However, the spiral mode of the prolate

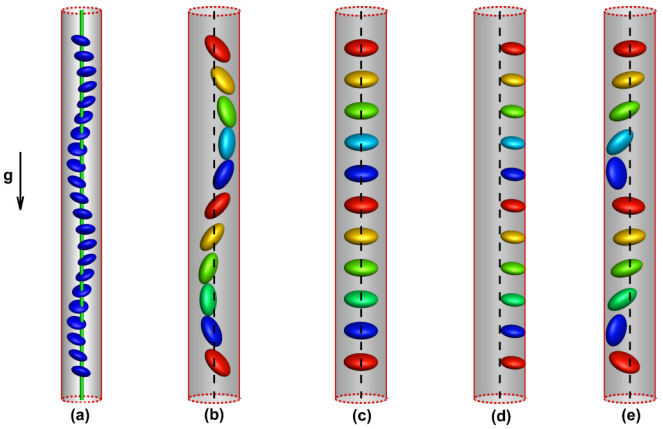

FIG. 4. (Color online) Snapshots of typical modes. (a) Spiral mode: The particle settles spirally around the tube axis; the inner green circular tube is drawn to guide the eye. (b) Oscillatory mode: The ellipsoid approaches two sides of the wall periodically and always settles inside an axis-symmetric plane. (c) Horizontal mode: The particle settles down horizontally along the tube axis. (d) Inclined mode: The ellipsoid settles off-axis with a constant inclination to the horizontal. (e) Anomalous mode: The ellipsoid periodically contacts one side of the tube wall and then approaches instead of migrates across the tube axis.

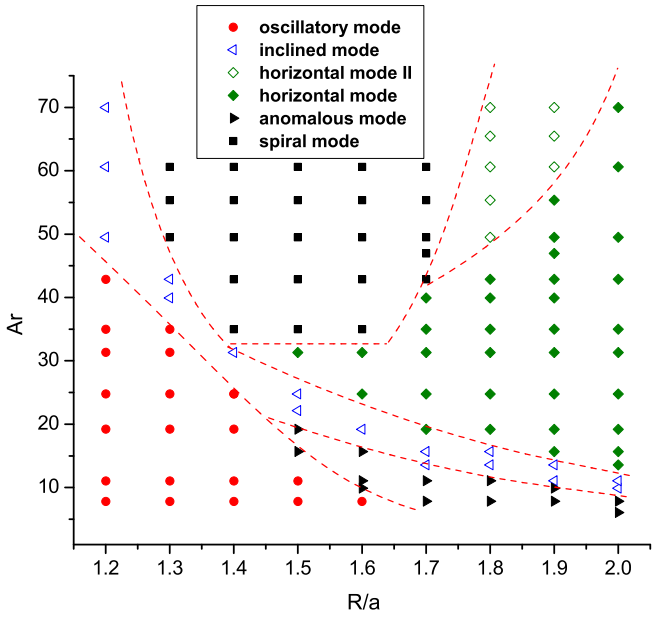

FIG. 5. (Color online) Phase diagram in the ($\frac{R}{a}$,Ar) plane. The dashed lines roughly show the borders of different regions.

ellipsoid occurs at $\frac{R}{a} < 1$ and higher Ar number [18]. For a larger $\frac{R}{a}$, the sedimentation mode may become the horizontal mode II, in which the ellipsoid settles down horizontally with small-amplitude oscillation. The geometric effect plays an important role in the mode transformation which will be discussed in the following sections. For wider tubes ($\frac{R}{a} \approx 1.8$), the horizontal mode occurs mainly when Ar is moderate. As Ar decreases, the inclined mode or the anomalous mode appears.

B. Details for sedimentation modes

For the spiral mode, the ellipsoid settles spirally around the tube axis, i.e., the z-axis, periodically [see Fig. 4(a)]. The angle γ between the x' axis and the z axis seems to be a constant and the particle itself does not rotate around the x' axis. The spiral mode occurs at a moderate confinement ratio($1.3 \leqslant \frac{R}{a} \leqslant 1.6$) and a higher Ar($\mathrm{Ar} \geqslant 35$). Figure 6 shows the evolutions of normalized x and y positions of the particle and the orientation of the x' axis. The length, time, and velocities are normalized by R, $\sqrt{\frac{g}{2a}}$, and $\sqrt{2ga}$, respectively. In Fig. 6(a), the distance between the center of the ellipsoid and the tube axis $r = \sqrt{x^2 + y^2}$ is also shown. It is seen that r is a constant in the spiral mode, i.e., the projection of the particle's trajectory in the (x, y) plane is a circle. From Fig. 6(b), it is also seen that the angle between the x' axis and the z axis, i.e., γ is almost a constant. For different cases, γ depends on $\frac{R}{a}$ and Ar. The angle γ increases with Ar but decreases with $\frac{R}{a}$ (see Fig. 7).

For the oscillatory mode, it seems that the ellipsoid "wiggles" down the tube [see Fig. 4(b)]. In this periodic mode, the ellipsoid approaches one side of the tube and then rotates (counterclockwise for the left side and clockwise for the right side) and migrates towards the other side when it is settling. The ellipsoid settles in an axis-symmetric plane,

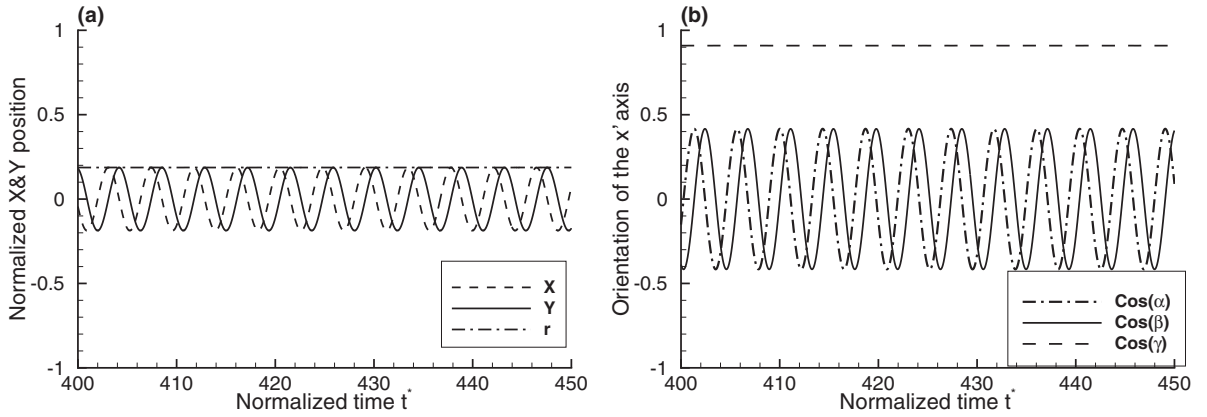

FIG. 6. Spiral mode ($\frac{R}{a} = 1.5$, Ar = 35). (a) The normalized x and y positions of the center of the particle; (b) the orientation of the x' axis as functions of time.

which depends on the initial position and orientation. For example, as shown in Fig. 8, the ellipsoid settles in the (y,z) plane and the x' axis is always perpendicular to the x axis. The oscillatory mode usually appears at $\frac{R}{a} \leqslant 1.6$ and Ar $\leqslant 31.3$.

For the horizontal mode, the ellipsoid settles along the tube axis, i.e., the x' axis overlaps with the z axis [Fig. 4(c)]. The horizontal mode most likely appears in wider tubes, i.e., at higher $\frac{R}{a}$. The force acting on the particle by the flow field is axis symmetric around the tube axis, so the total force is in the z direction and the resultant torque is zero. For a higher Ar, due to instability, the horizontal mode II may be observed. In the mode, the ellipsoid settles down horizontally but with small-amplitude oscillation. The ellipsoid may oscillate around tube axis in both the x and y directions with small amplitude [see Fig. 9(a)] and the x' axis no longer overlaps with the tube axis [see Fig. 9(b)].

For the inclined mode, the ellipsoid settles off-axis with a constant inclination to the horizontal [see Fig. 4(d)]. The angle between the x' axis and the horizontal and the off-axis amplitude are case dependent.

The anomalous mode is shown in Fig. 4(e) and Fig. 10. The ellipsoid migrates to and almost contact the left side wall of the tube and rolls counterclockwise when it is settling down. The particle approaches one side of wall periodically but is unable to across the tube axis to reach the other side. That significantly differs from the oscillatory mode shown in Fig. 8. Which side of the tube the ellipsoid will contact and which direction it rotates depend on the initial condition of the particle.

C. Further discussion on phase diagram

1. Inertia-induced mode transitions in a specific tube

As shown in Fig. 5, for a specific tube, e.g., $\frac{R}{a} = 1.9$, with Ar increasing, the anomalous mode, the inclined mode, the horizontal mode, and the horizontal mode II may appear.

At a small Ar, both the inertias of the particle and the fluid are small, so the particle is easier to oscillate in the tube and the anomalous mode appears. At a moderate Ar, a larger inertia of the particle may stabilize the movement of the particle. The ellipsoid may stop oscillating in the anomalous mode and turn to a more stable mode (the inclined mode). Further, with the inertia increasing, the horizontal mode instead of the incline mode may appear. For a higher Ar, for example, Ar $\geqslant 60.54$, the inertia of the particle increases and the settling velocity also increases. Hence, the Re of the fluid will increase and the fluid flow becomes unstable. Then the force exerted on the ellipsoid may be slightly not symmetric about the x' axis and the torque is no longer zero. Hence, the particle may oscillate with small amplitude [the horizontal mode II, see Fig. 11(a)]. It seems that the modes are determined by both the inertia of the particle and Re of the fluid flow.

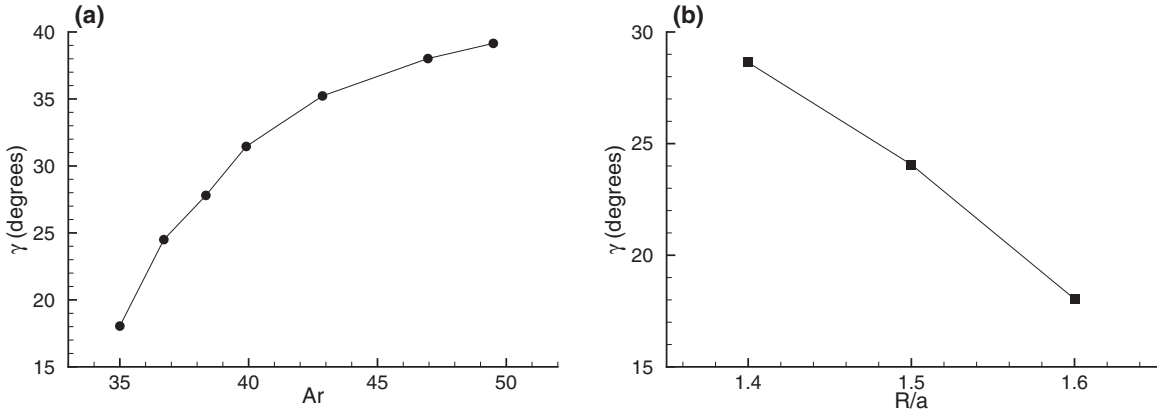

FIG. 7. In the spiral mode, (a) the angle γ as a function of Ar ($\frac{R}{a} = 1.6$) and (b) γ as a function of $\frac{R}{a}$ (Ar = 35).

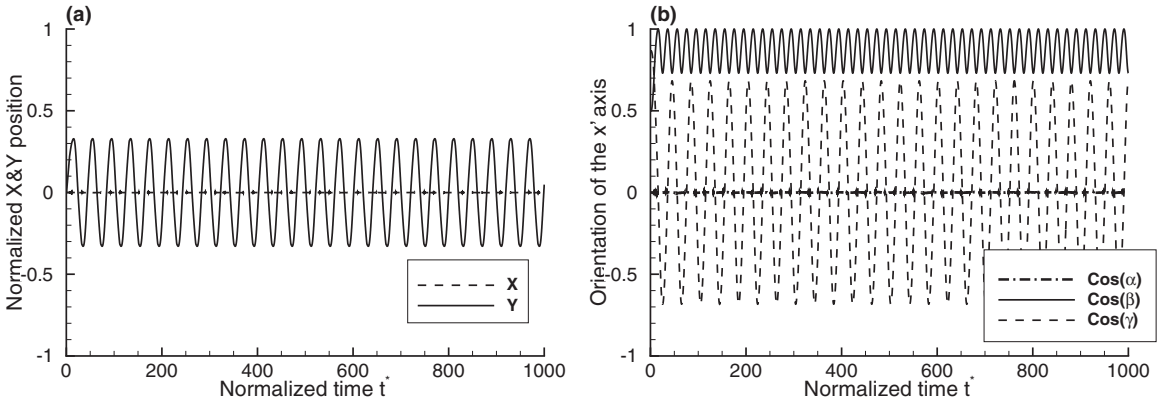

FIG. 8. Oscillatory mode ($\frac{R}{a} = 1.2$, Ar $= 11.07$). (a) The normalized x and y positions of the center of the particle as functions of time. (b) The orientation of the x' axis as a function of time.

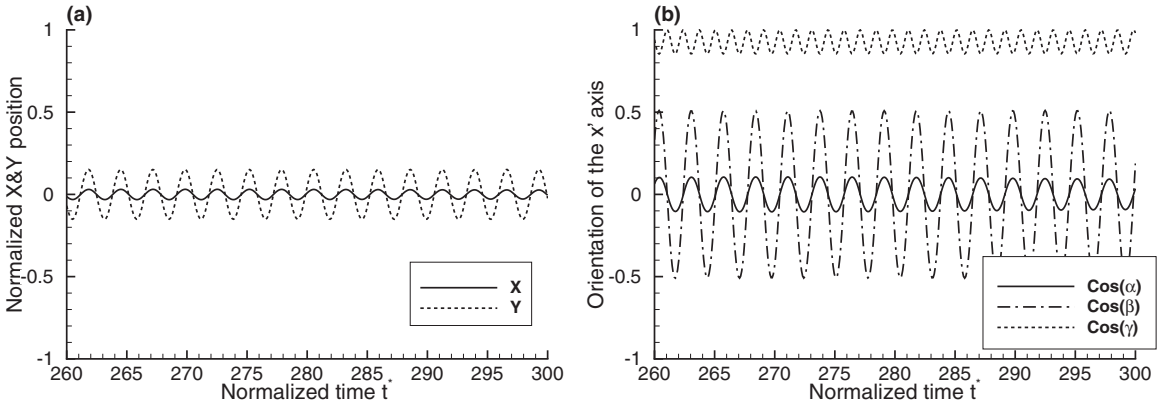

FIG. 9. Horizontal mode II ($\frac{R}{a} = 1.8$, Ar $= 60.62$). (a) The normalized x and y as functions of time. (b) The orientation of the x' axis as a function of time.

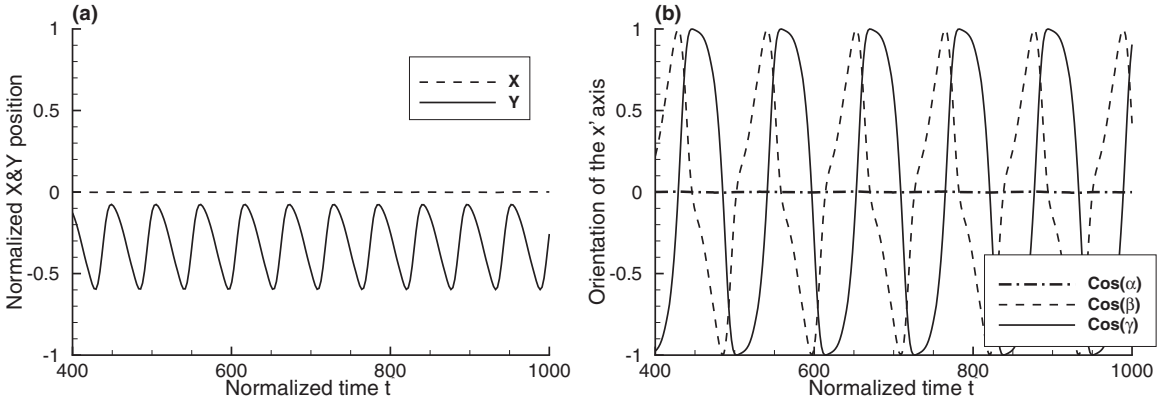

FIG. 10. Anomalous mode ($\frac{R}{a} = 1.7$, Ar $= 11.07$). (a) The normalized x and y positions of the center of the particle. (b) The orientation of the x' axis.

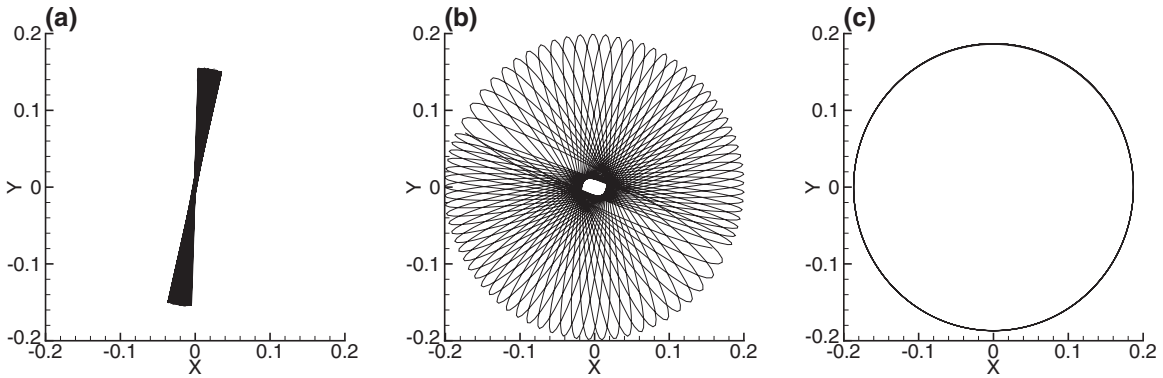

FIG. 11. Top views of the trajectories of the particle's center. (a) The horizontal mode II with $\frac{R}{a} = 1.8, \mathrm{Ar} = 60.62$. (b) The intermediate state for case $\frac{R}{a} = 1.7, \mathrm{Ar} = 60.62$, $t^* \leqslant 400$ and (c) the terminal state ($t^* \geqslant 800$) for case $\frac{R}{a} = 1.7, \mathrm{Ar} = 60.62$.

2. *Transition from the horizontal mode II to the spiral mode*

At a higher Ar and $\frac{R}{a}$, the particle may settle down horizontally with small oscillations (the horizontal mode II). For the mode, the top-view of the trajectory in the (x,y) plane is almost a line with small-amplitude oscillations in the circumferential direction [see Fig. 11(a)]. For cases with higher Ar and narrower tube $\frac{R}{a} \approx 1.7$, the horizontal mode II may transfer to the spiral mode due to the stronger wall effect. Figure 11(c) shows the terminal top view of the trajectory in the (x,y) plane for the spiral mode. It is a circle, i.e., the particle only moves in the circumferential direction.

For the case $\frac{R}{a} = 1.7, \mathrm{Ar} = 60.62$, it may take long time for the particle to develop to the perfect spiral mode. An intermediate state is shown in Fig. 11(b). It is a top view of the trajectory. At this intermediate state the ellipsoid not only oscillates in the radial direction but also moves along the circumferential direction. In both experimental studies for a falling disk [8] and a rising disk [27], similar top views of the trajectory were observed. Hence, the horizontal mode would transfer to the spiral mode when the tube is narrower.

The transition can be understood in the following way. When the particle settles down, there is a vortex that is attached to the particle in the wake due to shear stress. In a wider tube ($R/a > 2$), the wake regime is steady and axisymmetric in the center of the tube. The wake is almost not affected by the tube wall. The particle adopts the horizontal mode. However, when the tube becomes narrower ($R/a \approx 1.8$), the wake interacts with two sides of the tube wall and triggers the radial instability. The particle may move (oscillate) mainly in radial direction with a negligible oscillation in the circumferential direction. That is the horizontal mode II. When the tube is much narrower ($R/a \approx 1.7$), due to the strong interaction between the wake and the tube wall, the circumferential instability and movement become dominant, then the particle adopts the spiral mode.

3. *Comparison between the oscillatory mode and the anomalous mode*

The anomalous mode instead of the oscillatory mode occurs when $\frac{R}{a} > 1.5$ and $\mathrm{Ar} \approx 10$ (see Fig. 5). Although the sedimentation pattern looks similar in the oscillatory and anomalous modes (see Fig. 4), there are some differences. One significant difference is that in the oscillatory mode instead of the anomalous mode, the ellipsoid migrates and crosses the tube axis from one side of the tube to the other side.

In the follows, the two modes that settle in the (y,z) plane are compared. The position, velocity, and force in the y direction for the anomalous mode and the oscillatory mode are shown in Figs. 12(a)–12(c) and 12(d)–12(e), respectively. In each subfigure, evolution of two periods of the sedimentation is shown. In the anomalous mode, at point a, the velocity is zero and the displacement between the tube axis and ellipsoid center reaches a maximum value. In the moment, the force acting on the particle reaches a maximum value (in the $-y$ direction). Due to the force, the particle moves towards the tube axis with acceleration (the movement and force directions are consistent). At point b, the velocity reaches a maximum value and the force exerted on the particle is zero. Although the force reverses its direction (the $+y$ direction) after point b, the particle still moves towards the tube axis (the $-y$ direction). However at time c, although the particle is very close to the tube axis, it is unable to across the axis. After time c, the particle migrates towards the wall where it just comes from. As a result, the anomalous mode will appear.

For the oscillatory mode [see Fig. 12(d), 12(e), and 12(f)], the procedure from points d to e looks similar to that from points a to c in the anomalous mode. However, at point e, the particle is at the tube axis while at point c the particle is only close to the tube axis. For the velocity, it is not zero at point e but zero at point c. In the mode, after it crosses the tube axis, it will continue to migrate towards the other side of the tube. Then the oscillatory mode will appear. The geometric effect of the tube may play an important role to determine the sedimentation mode.

In the parameter regime, the oscillatory mode appears in the left lower part of the phase diagram (smaller $\frac{R}{a}$ and smaller Ar number) and the anomalous mode appears when tube is wider with smaller Ar number. It seems straightforward to understand the two modes in the phase diagram. For a narrow tube, due to the inertia of the particle, the particle's velocity may not reduce to zero before it reaches the tube axis and it is easy to cross the axis to the other side of the tube. However, in a wider tube, the particle may be difficult to cross the tube axis.

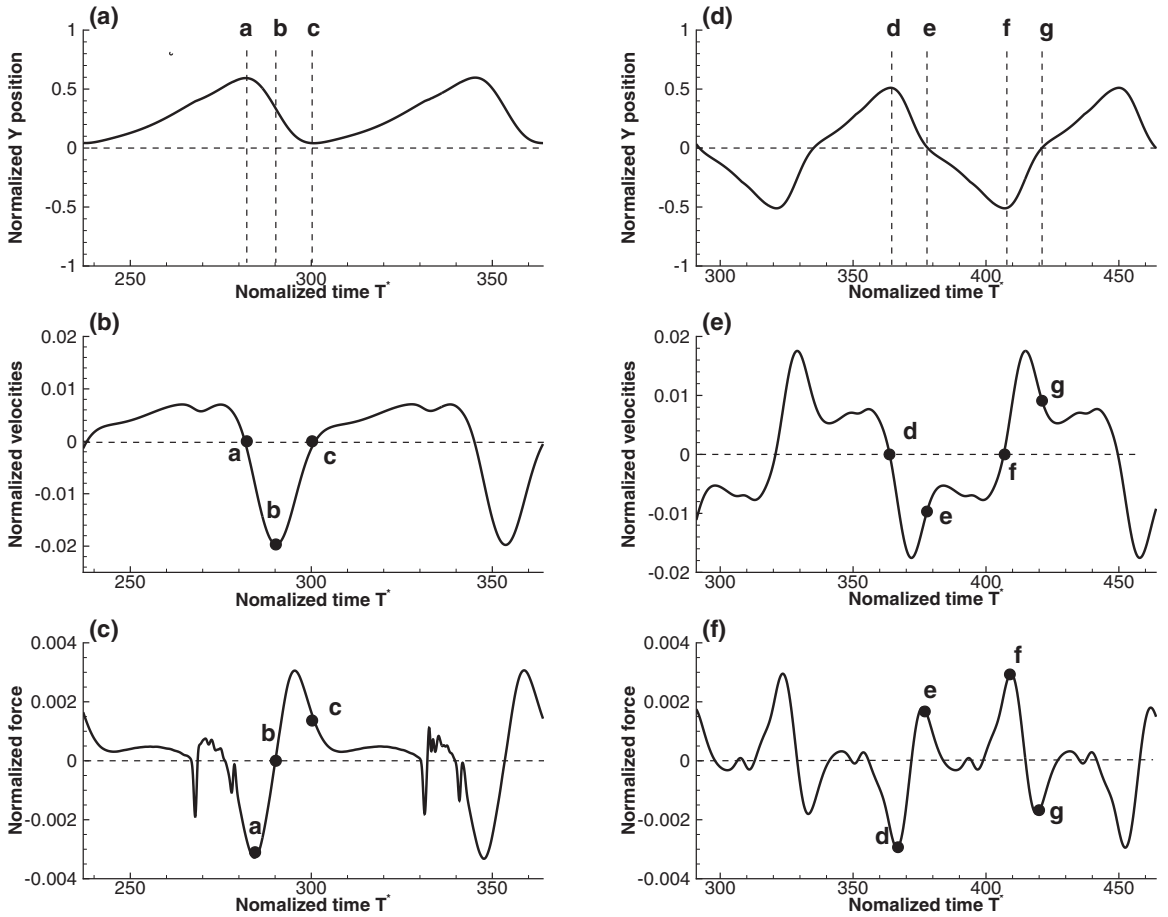

FIG. 12. Anomalous mode and oscillatory mode. [(a)–(c)] Position, velocity, and force acting on the ellipsoid as functions of time in the anomalous mode. [(d)–(f)] Those in the oscillatory mode.

D. Drag coefficient and terminal Reynolds number

To evaluate the drag force effect in the sedimentation, we calculated the drag coefficient C_d, which is defined as

$$C_d = \frac{F_d}{\frac{1}{2}\rho_f S U_t^2} = \frac{\Delta\rho V g}{\frac{1}{2}\rho_f S U_t^2} = \frac{\frac{4}{3}\pi abc\Delta\rho g}{\frac{1}{2}\rho_f S U_t^2}, \qquad (11)$$

where F_d is the average drag force and V represents the volume of the particle. U_t is the average terminal settling velocity and S denotes the effective area, i.e., the projected area of the ellipsoid in the (x, y) plane. Figure 13 shows the drag coefficient C_d as a function of Ar. Each line represents a specific confinement ratio. It suggests that for a specific $\frac{R}{a}$, C_d decreases with Ar. For a fixed Ar, C_d usually decreases with $\frac{R}{a}$. That is, usually the narrower the tube is, the larger the drag force exerted on the ellipsoid. It also hints that usually the particle settles slower in narrower tubes. However, there is an exception. For example, when $31.3 \leqslant \mathrm{Ar} \leqslant 39.9$, C_ds calculated from cases $\frac{R}{a} = 1.4$ are larger than those from cases $\frac{R}{a} = 1.2$. Hence, as shown in the region between the two

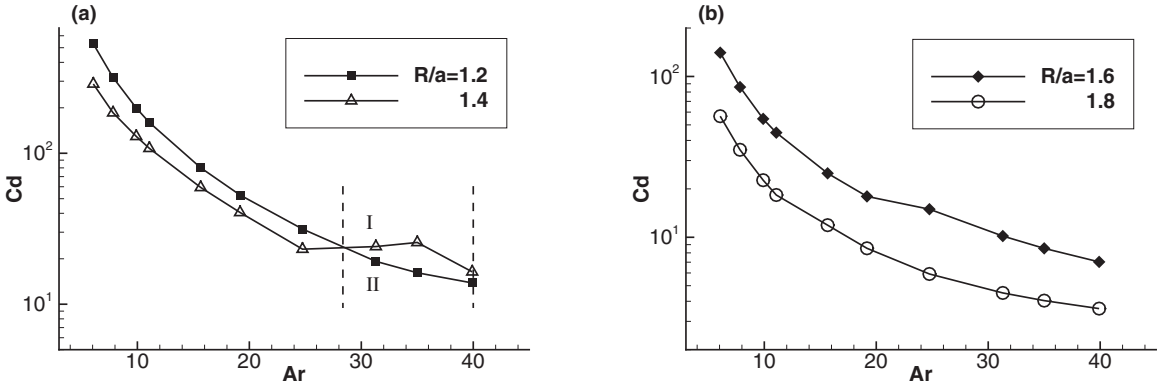

FIG. 13. Drag coefficient C_d as a function of Ar with different confinement ratio $1.2 \leqslant \frac{R}{a} \leqslant 1.8$.

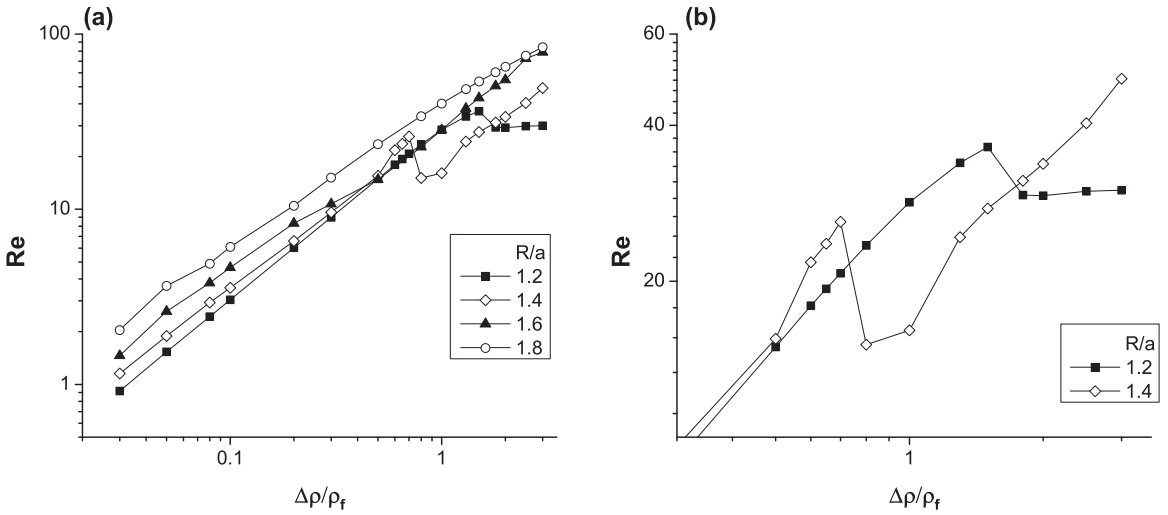

FIG. 14. Terminal Re as a function of $\frac{\Delta\rho}{\rho_f}$.

dashed lines in Fig. 13(a), for the specific Ar $\in$ (31.3,39.9), the particle settles in narrower tube ($\frac{R}{a} = 1.2$) faster than it settles in wider tube ($\frac{R}{a} = 1.4$).

The exception may be due to the mode difference. For example, in Case I [wider tube, $\frac{R}{a} = 1.4$ and Ar = 31.0, see Fig. 13(a)] and Case II (narrower tube, $\frac{R}{a} = 1.2$ and Ar = 31.0), the particles adopt the inclined mode and oscillatory mode, respectively. In the inclined mode, the orientation of the particle is always almost horizontal. By contrast, in the oscillatory mode, its orientation changes periodically from vertical to inclined. In Case II, the average effective area S_{II} in a period is about 52.8% of the effect area S_{I} in Case I, i.e., $\frac{S_{\mathrm{II}}}{S_{\mathrm{I}}} = 0.528$. In the meanwhile, the average settling velocity in Case II is 1.56 times higher than that in Case I, i.e., $\frac{U_{\mathrm{II}}}{U_{\mathrm{I}}} = 1.56$. Hence, according to Eq. (11), $\frac{(C_d)_{\mathrm{I}}}{(C_d)_{\mathrm{II}}} = (\frac{U_{\mathrm{II}}}{U_{\mathrm{I}}})^2 \frac{S_{\mathrm{II}}}{S_{\mathrm{I}}} = 1.29$, i.e., the C_d in Case I is 1.29 times larger than that in Case II. Hence, the mode difference contributes to the bump in the plot, i.e., the region 31.3 $\leqslant$ Ar $\leqslant$ 39.9 in Fig. 13(a).

Figure 14 shows the terminal Re as a function of $\frac{\Delta\rho}{\rho_f}$ and Fig. 14(b) is a zoom-in view of Fig. 14(a) with $\frac{R}{a} = 1.2$, 1.4. From Fig. 14(a), it is seen that, on the whole, Re increases with both $\frac{\Delta\rho}{\rho_f}$ and $\frac{R}{a}$. However, again there is an exception, i.e., the Re for narrow tubes (e.g., $\frac{R}{a} = 1.2$) is larger than that for wider tubes (e.g., $\frac{R}{a} = 1.4$) due to different modes. The exception is consistent with the exception in the C_d curves shown in Fig. 14(b).

It is also shown that at $\frac{\Delta\rho}{\rho} \approx 0.75$, $\frac{R}{a} = 1.4$, the lighter particle may settle faster than the heavy one, which is also attribute to mode difference.

E. Settling velocities in unconstrained and constrained cases

To explore the mechanism why the particle adopts a specific mode under a certain circumstance instead of the other possible modes, some constrained cases with steady modes (the horizontal and inclined modes) are simulated.

It is difficult to specify the periodic modes (the anomalous mode, the oscillatory mode, the spiral mode, and the horizontal II mode) due to the orbit and orientation of the particle are complicated functions of time. Hence, in the constrained simulations, only simple steady modes (the horizontal mode or the inclined mode) are considered.

When a particle is supposed to follow the horizontal mode, the particle is only allowed to move along the tube axis horizontally. Its rotation and lateral migration are suppressed. Then the constrained motion is the horizontal mode and the particle will reach a constant settling velocity.

Six cases with different original modes and their corresponding constrained cases are simulated. The parameters $\frac{R}{a}$ and Ar are shown in the second and third columns in Table III. For example, in Case A, $\frac{R}{a} = 1.6$ and Ar = 35, the unconstrained mode is the spiral mode and it is referred to as the original mode. The details for specifying the corresponding horizontal mode are illustrated in the last paragraph. To specify the constrained inclined mode, it is not straightforward to specify the inclined angle γ and the distance away from the tube axis r_d. The γ and r_d come from the closest inclined state with same $\frac{R}{a}$ in the phase diagram. For example, for Case A ($\frac{R}{a} = 1.6$ and Ar = 35), the closest case with the inclined mode is approximately at $\frac{R}{a} = 1.6$ and Ar = 20. The γ and r_d from the inclined case ($\frac{R}{a} = 1.6$ and Ar = 20), i.e., $\gamma = 18.4^\circ$ and $r_d = 0.25$ are adopted.

TABLE III. Normalized terminal settling velocities for unconstrained (terminal velocity U_0 for the original mode) and constrained cases (U_1 for the horizontal mode and U_2 for the inclined mode). Velocities are normalized by $\sqrt{2ga}$.

Case	$\frac{R}{a}$	Ar	Original mode	U_0	U_1	U_2
A	1.6	35	Spiral mode	0.2865	0.2706	0.2793
B	1.8	11.07	Anomalous mode	0.0601	0.0467	0.0545
C	1.4	11.07	Oscillatory mode	0.0361	0.0158	0.0284
D	1.8	60.62	Horizontal II	0.7159	0.6917	None
E	1.9	11.07	Inclined mode	0.0615	0.0544	None
F	1.9	24.75	Horizontal mode	0.2397	None	0.2098

We also observed that if the particle is constrained with the x' axis perpendicular to the tube axis, i.e., it settles down with smallest projected area in the (x,y) plane along the tube axis, the settling velocity reaches the largest. However, this mode is not observed. Here all of the possible modes do not include this artificial mode.

The terminal settling velocities for these unconstrained (U_0) and constrained cases (U_1 and U_2) are shown in Table III. It is seen that for all cases, the terminal velocity of its original mode (U_0) is larger than those of the constrained modes (U_1 for the horizontal and U_2 for the inclined mode). With limited observations (Cases A to F), we conclude that the particle settles faster in the unconstrained modes than in the corresponding constrained modes. It is conjectured that the particle tends to adopt the mode with the largest settling velocity among the six modes that we found.

V. CONCLUSION

The sedimentation of an oblate ellipsoidal particle inside narrow tubes has been studied numerically. Several typical periodic and steady sedimentation modes are identified. It is not found that the modes depend on the initial orientation or position. The phase diagram as a function of the confinement ration $\frac{R}{a}$ and Ar is achieved. From the phase diagram, it is observed that the anomalous mode appears in the region with small Ar. Through comparisons between the anomalous and oscillatory modes, it is identified that the geometric effect of the tube plays a critical role in the anomalous mode.

Usually, an oblate particle settles faster in a wider tube; in a specific tube, a heavier particle settles faster. However, unusual cases are observed in our simulated results. In the mode transitional region with $\frac{R}{a} = 1.4$ and $\frac{\Delta\rho}{\rho_f} \approx 0.8$, a lighter particle may settle faster than a heavier one. For Ar ≈ 35, the particle settles faster in a narrow tube($\frac{R}{a} = 1.2$) than in a wider tube ($\frac{R}{a} = 1.4$) due to different modes.

Some constrained cases with two steady modes are simulated. With limited observations, we found that the particle settles faster in the unconstrained modes than in the corresponding constrained modes. This might inspire further study on why the particle adopts a specific mode under a certain circumstance.

ACKNOWLEDGMENTS

H.H. was supported by the National Natural Science Foundation of China (Grant No. 11172297), the Anhui Provincial Natural Science Foundation (Grant No. 1308085MA06), the Fundamental Research Funds for the Central Universities, and the Program for New Century Excellent Talents in University, Ministry of Education, China (NCET-12-0506).

[1] M. Sugihara-Seki, J. Fluid Mech. **324**, 287 (1996).
[2] Z. Wang, Y. Sui, P. D. M. Spelt, and W. Wang, Phys. Rev. E **88**, 053021 (2013).
[3] D. R. Mikulencak and J. F. Morris, J. Fluid Mech. **520**, 215 (2004).
[4] Z. Yu, N. Phan-Thien, and R. I. Tanner, J. Fluid Mech. **518**, 61 (2004).
[5] G. Segre and A. Silberberg, Nature **189**, 209 (1961).
[6] S. Jung, S. E. Spagnolie, K. Parikh, M. Shelley, and A.-K. Tornberg, Phys. Rev. E **74**, 035302 (2006).
[7] W. Russel, E. Hinch, L. Leal, and G. Tieffenbruck, J. Fluid Mech. **83**, 273 (1977).
[8] H. Zhong, S. Chen, and C. Lee, Phys. Fluids **23**, 011702 (2011).
[9] M. Rahmani and A. Wachs, Phys. Fluids **26**, 083301 (2014).
[10] G. B. Jeffery, Proc. Royal Soc. London A **102**, 161 (1922).
[11] Z. Yu, N. Phan-Thien, and R. I. Tanner, Phys. Rev. E **76**, 026310 (2007).
[12] H. Huang, X. Yang, M. Krafczyk, and X.-Y. Lu, J. Fluid Mech. **692**, 369 (2012).
[13] T. Rosén, M. Do-Quang, C. K. Aidun, and F. Lundell, Phys. Rev. E **91**, 053017 (2015).
[14] H. Huang, Y. F. Wu, and X. Lu, Phys. Rev. E **86**, 046305 (2012).
[15] Z. Xia, K. W. Connington, S. Rapaka, P. Yue, J. J. Feng, and S. Chen, J. Fluid Mech. **625**, 249 (2009).
[16] J. Feng, H. H. Hu, and D. D. Joseph, J. Fluid Mech. **261**, 95 (1994).
[17] T. Swaminathan, K. Mukundakrishnan, and H. H. Hu, J. Fluid Mech. **551**, 357 (2006).
[18] H. Huang, X. Yang, and X.-Y. Lu, Phys. Fluids **26**, 053302 (2014).
[19] D. d'Humières, Philos. T. R. Soc. A **360**, 437 (2002).
[20] C. K. Aidun, Y. Lu, and E.-J. Ding, J. Fluid Mech. **373**, 287 (1998).
[21] E. Ding, C. K. Aidun *et al.*, J. Fluid Mech. **423**, 317 (2000).
[22] D. Qi and L.-S. Luo, J. Fluid Mech. **477**, 201 (2003).
[23] P. Lallemand and L.-S. Luo, J. Comput. Phys. **184**, 406 (2003).
[24] D. Qi, J. Fluid Mech. **385**, 41 (1999).
[25] A. Karnis, H. Goldsmith, and S. Mason, Can. J. Chem. Eng. **44**, 181 (1966).
[26] B. Yang, J. Wang, D. Joseph, H. H. Hu, T.-W. Pan, and R. Glowinski, J. Fluid Mech. **540**, 109 (2005).
[27] P. C. Fernandes, F. Risso, P. Ern, and J. Magnaudet, J. Fluid Mech. **573**, 479 (2007).